PCCP

PAPER

View Article Online
View Journal | View Issue

Cite this: *Phys. Chem. Chem. Phys.*, 2014, **16**, 26631

The effects of 1-pentyne hydrogenation on the atomic structures of size-selected Au_N and Pd_N (N = 923 and 2057) nanoclusters†

Kuo-Juei Hu,[a] Simon R. Plant,[a] Peter R. Ellis,[b] Christopher M. Brown,[b] Peter T. Bishop[b] and Richard E. Palmer*[a]

Received 18th June 2014,
Accepted 24th September 2014

DOI: 10.1039/c4cp02686a

www.rsc.org/pccp

We report an investigation into the effects of the vapour-phase hydrogenation of 1-pentyne on the atomic structures of size-selected Au and Pd nanoclusters supported on amorphous carbon films. We use aberration-corrected high-angle annular dark field (HAADF) scanning transmission electron microscopy (STEM) to image populations of the nanoclusters at atomic resolution, both before and after the reaction, and we assign their atomic structures by comparison with multi-slice image simulations over a full range of cluster orientations. Gold nanoclusters consisting of 923 ± 20 and 2057 ± 45 atoms are found to be robust, exhibiting high structural stability. However, a significant portion of $Pd_{923\pm26}$ nanoclusters that appear amorphous prior to treatment are found to exhibit high symmetry structures post-reaction, which is interpreted as the reduction of oxidised Pd nanoclusters under the reaction conditions.

1 Introduction

It has long been established that the catalytic properties of supported metal particles vary as a function of size.[1] The use of size-selected metal nanoclusters as model catalysts[2–8] is one of the routes that has enabled catalytic activity to be accurately related to particle size. However, it is not just the size, but the full atomic structure which can regulate the performance of a catalyst, since catalytic activity can, in some cases, be correlated with specific reactive sites at the catalyst particle surface.[9] Indeed, it has been demonstrated that controlling particle shape may enable improved selectivity.[10] As a result, it is vital to gain an understanding of the effects upon the structure of such model catalysts arising from exposure to realistic reaction conditions, in order to achieve more robust catalyst design with improved performance. A number of techniques have been used to monitor nanocluster or nanoparticle catalysts subject to reaction conditions, including, for instance, *in situ* TEM,[11–13] electron tomography[14] and *in situ* STM.[15] Aberration-corrected HAADF-STEM has previously been used to identify catalytically-active Au nanoclusters on oxide supports,[16] and the catalytic activity of size-selected Au nanoclusters on oxides is well-established.[17] For instance, amongst size-selected Au nanoclusters, Au_{55} has been highlighted as a high performance catalyst with pronounced oxidation resistance.[18] HAADF-STEM imaging of size-selected Au nanoclusters on amorphous carbon has enabled the elucidation of their three-dimensional atomic structures.[19] Nanoclusters of a specific size can exhibit a range of atomic structures that differ significantly from the bulk, and multi-slice image simulations have facilitated the identification of structures from HAADF-STEM images for size-selected Au_{20},[20] Au_{55},[21] Au_{309} (ref. 19) and Au_{923},[22–24] regardless of cluster orientation on the substrate. Given the recent demonstration of atomic structure control during the formation of size-selected Au_{923},[24] there is now a great potential to study the catalytic properties of such nanoclusters not only as a function of their size, but also atomic configuration, under realistic reaction conditions. Size-selected Pd_N nanoclusters (N = 55–400) supported on graphite have already been studied under such conditions for methane oxidation[25] and 1-pentyne hydrogenation.[26] The largest nanoclusters in this size range (especially Pd_{400}) exhibited very high selectivity to the hydrogenation of 1-pentyne in the vapour phase, thus motivating the study of still larger nanocluster sizes.

The selective hydrogenation of alkynes is relevant to both Au[27–29] and Pd catalysts.[26,30–33] The vapour-phase 1-pentyne hydrogenation reaction over Pd supported on θ-Al_2O_3 reveals incorporation of carbon into the catalyst to provide a Pd–C phase believed to be active for selective hydrogenation,[31] and indeed, the incorporation of carbon and hydrogen into the

[a] *Nanoscale Physics Research Laboratory, School of Physics and Astronomy, University of Birmingham, Birmingham, B15 2TT, UK. E-mail: R.E.Palmer@bham.ac.uk*
[b] *Johnson Matthey Technology Centre, Blounts Court Road, Sonning Common, Reading, RG4 9NH, UK*

† Electronic supplementary information (ESI) available. See DOI: 10.1039/c4cp02686a

surface has been shown to control hydrogenation events at the surface.[32] However, Pd catalysts can also become deactivated and degraded by such processes.[34] Aging of the catalyst as a result of thermally- or chemically-driven restructuring[35–37] is important for both the catalytic activity and stability. It is therefore crucial to be able to identify changes in the structure and composition of such catalytic particles both *before* and *after* exposure to realistic reaction conditions, in order to achieve catalysts with optimised efficiency, selectivity and sustained performance.

Here, we report the atomic structures of size-selected Au and Pd nanoclusters (containing 923 and 2057 atoms) supported on amorphous carbon films, both before and after exposure to the thermal and chemical conditions for the 1-pentyne hydrogenation reaction. Observations made *ex situ* using aberration-corrected HAADF-STEM provide direct geometric information about these nanoclusters. Multi-slice HAADF-STEM image simulations are compared with experimental images to identify the atomic structures of the observed nanoclusters, over a full range of orientations on the substrate. Our results show that the Au nanoclusters of both sizes are very stable under the reaction conditions, remaining largely unchanged after pure thermal treatment and after full exposure to the chemical reaction conditions. However, a notable proportion of Pd_{923} nanoclusters, of which the vast majority (97%) appear amorphous before the reaction, are found to exhibit a face-centred cubic structure after treatment.

2 Experimental section

Gold and palladium nanoclusters were generated using a magnetron-sputtering gas-condensation cluster beam source.[38,39] A lateral time-of-flight mass filter[40] connected to the source permits accurate size selection prior to deposition of the nanoclusters in high vacuum conditions (10^{-7}–10^{-6} mbar). Based on calibration with Ar^+, the nominal mass resolutions employed were $M/\Delta M \approx 18$ and $M/\Delta M \approx 23$ for Pd and Au nanoclusters, respectively, resulting in nanoclusters that consist of 923 ± 26 and 2057 ± 57 atoms for Pd, and 923 ± 20 and 2057 ± 45 atoms for Au. The size-selected nanoclusters were deposited (at energies in the range 0.4–0.9 eV per atom) directly onto amorphous carbon films supported on molybdenum TEM grids. Following deposition, the supported Au nanoclusters were brought into air (ambient conditions) and then transferred into a vacuum desiccator for storage, both before and after imaging and treatment. Transfer of the supported Au nanoclusters from the vacuum desiccator to the microscope (in ambient conditions) was performed within ~20 minutes. The Pd nanoclusters were stored in a desiccator at ambient temperature and pressure for 100 days prior to initial imaging, and the reaction exposure was conducted within a further 10 days. Imaging was then performed 20 days after the reaction. The samples were transferred in ambient conditions for imaging and treatment. For 1-pentyne hydrogenation treatment, each of the TEM grids was transferred into a quartz tube (length 360 mm, inner diameter 4 mm) and held at the centre of the tube by means of a quartz wool plug. A flow of pure He gas (279 ml min^{-1}) was used to provide an inert atmosphere when investigating the effects of the thermal annealing. For the hydrogenation reaction, the carrier gas consisted of 40% H_2/60% He (flow rate of 247 ml min^{-1}). In the reaction, this carrier gas was used to vaporise a reagent solution comprising 1 M 1-pentyne plus 1 M 2-methylpentane (used in such reactions as an internal standard for gas chromatography[26]) dissolved in *n*-hexane. The temperature was increased at a rate of 2 °C min^{-1} from room temperature to 250 °C and then maintained at constant temperature for 2 hours. At the end of the treatment, the carrier gas was switched to pure He, and the sample was allowed to cool for 30 minutes. Atomic resolution imaging was carried out using a JEOL 2100F STEM operating at 200 keV and equipped with a spherical aberration probe corrector (CEOS GmbH) and high-angle annular dark field (HAADF) detector. The inner and outer collection angles of the HAADF detector were 62 and 164 mrad, respectively.[41] Imaging was performed so as to avoid beam damage to the atomic structures of the nanoclusters (see ESI†). Following imaging, high symmetry nanocluster structures were identified by comparing experimental images with an atlas of multi-slice image simulations over a full range of orientations in three dimensions. Simulations of Au_{2057}, Pd_{923} and Pd_{2057} were generated using the QSTEM package.[42] The previously published simulation atlas was used in the case of Au_{923}.[22]

3 Results and discussion

The high symmetry isomers of the nanoclusters observed in this study display structural motifs that are characteristic of the icosahedron (Ih), Ino-decahedron (Dh) and face-centred cubic (FCC) polyhedron, just as for size-selected Au_{923} nanoclusters studied previously.[22–24] Fig. 1 shows typical HAADF-STEM images and corresponding multi-slice image simulations of an illustrative set of high symmetry Au_{2057} isomers. There is always a proportion of nanoclusters within a sample population that cannot be assigned uniquely to a high symmetry structure, while some nanoclusters appear to be completely amorphous, and we designate such structures as being amorphous or unidentified (A/U). In the present study, the Dh-Au_{923} and Dh-Au_{2057} nanoclusters are found to be the most abundant; recent experimental investigations of Au_{923} suggest that Dh-Au_{923} is a low energy structure in this size regime, whereas Ih-Au_{923} in particular is metastable.[22,24]

Several factors might induce changes in the structure of nanoclusters in the continuous flow vapour-phase reaction. For example, thermal annealing alone can be an important driving force in triggering the structural transformation of nanoparticles.[36,37,43] In order to de-couple any effects of (mere) elevated temperatures from the full reaction conditions, thermal annealing was first conducted on Au_{923} and Au_{2057} nanoclusters. Since recent work shows that the relative proportions of isomers within a sample population can be controlled by tuning the formation parameters for the generation of Au_{923},[24] samples were produced using identical formation conditions in the

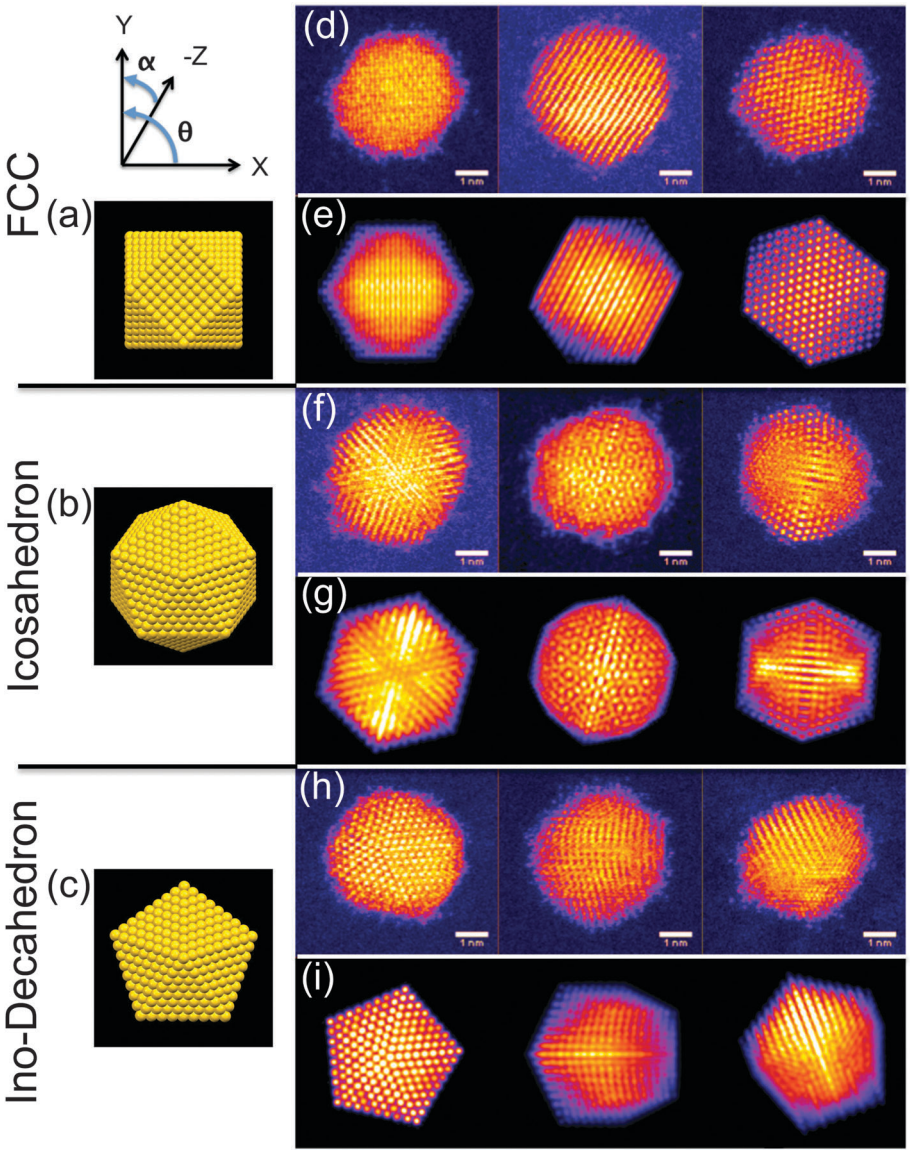

Fig. 1 Models of the atomic structures for the (a) face-centred cubic (cuboctahedron shown), (b) icosahedral, and (c) Ino-decahedral isomers of Au_{2057}, viewed at $\theta = 0°$, $\alpha = 0°$, as defined by the axes shown. Typical HAADF-STEM images of Au_{2057} nanoclusters (top) with corresponding multi-slice image simulations (below) for: (d, e) the face-centered cubic (FCC) polyhedron, (simulation orientations in row (e), from left to right, are along $\theta = 45°$, $\alpha = 45°$, and $\theta = 0°$, $\alpha = 30°$, and the 110 axis), (f, g) the icosahedron (Ih) (simulation orientations in row (g) from left to right are normal to (111) facet, along the 5-fold axis, and along the 2-fold axis), and (h, i) the Ino-decahedron (Dh) (simulation orientations in row (i) from left to right are along 5-fold axis, at $\theta = 0°$, $\alpha = 50°$, and at $\theta = 0°$, $\alpha = 30°$).

cluster beam source (parameters are detailed in the figure captions). Fig. 2 shows a comparison of the proportions of Au_{923} isomers, before and after thermal annealing at 523 K for 2 hours in different atmospheres. (The results for Au_{2057} nanoclusters are very similar to those shown in Fig. 2, and are provided in the ESI.†) Fig. 2(a) presents charts showing the combined results for all 3 samples of Au_{923} nanoclusters prior to thermal annealing. In general, the error bars shown on the bar charts are related to the Poisson error. However, the error bars shown on the bar chart in Fig. 2(a) derive from the standard error for the 3 samples. Fig. 2(b) shows the proportions of Au_{923} isomers following storage in a vacuum desiccator, where the sample has been imaged within 14 days of preparation, while Fig. 2(c) and (d) show the result of heating in a pure He gas flow, and in a gas flow of 40% H_2/60% He, respectively. Although some slight variations in isomer distributions can be observed, there are no significant changes in the Au_{923} (or Au_{2057}) isomers as a result of subjecting them to these conditions.

The results may be explained by considering the temperatures required to induce melting in gold nanoparticles as a function of particle size. Thermal annealing in an inert atmosphere can be interpreted as a rapid process of bringing nanoclusters into a state of thermal equilibrium, where no reactants are involved. According to previous studies,[36] the Ih-to-Dh structural transformation can occur for particles in the size range from 3 nm to 14 nm without having to reach the melting point. For instance, the gap between transition temperature and melting point is predicted to be ~100 K for a Au particle size of 4 nm, based on

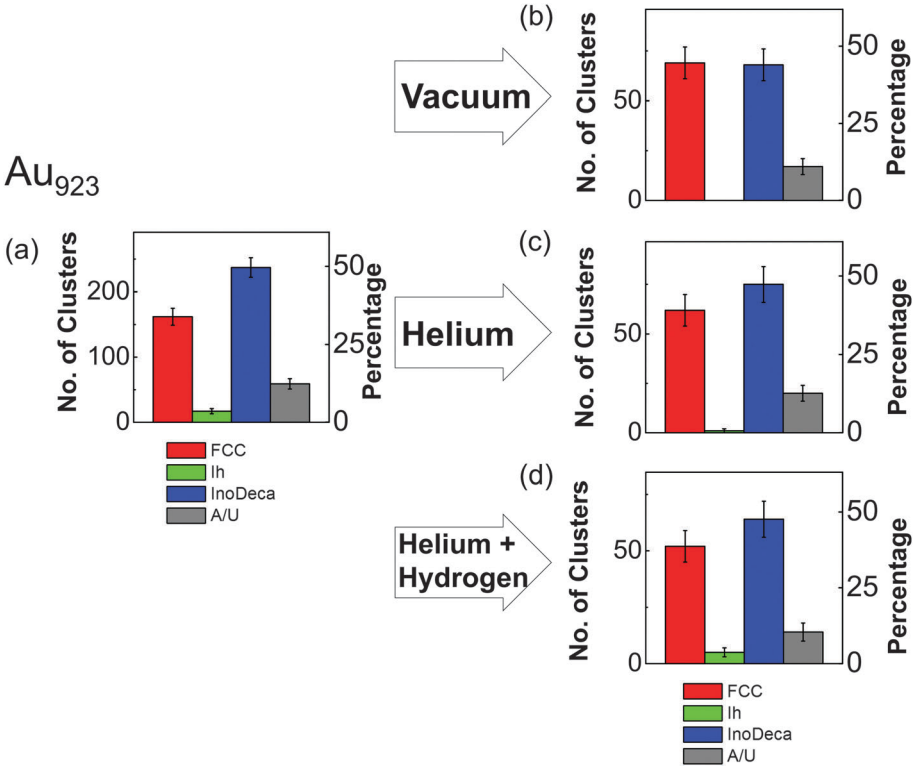

Fig. 2 Charts showing the relative proportions of Au_{923} isomers (a) before thermal treatment, (b) after storage in vacuum at RT, (c) after thermal treatment under a gas flow of pure He (279 ml min^{-1}), and (d) after thermal treatment under a gas flow of 40% H_2 + 60% He (247 ml min^{-1}). Thermal treatment was conducted at 523 K for 2 hours (ramp rate of 2 °C min^{-1} from RT). Related cluster formation parameters: condensation length, 250 mm; magnetron sputtering power, 10 W DC; condensation pressure, 0.60 mbar; condensation gas flows, rate 200 sccm (Ar) and 150 sccm (He); deposition energy, 0.5 eV per atom.

the extrapolation from experimental data.[36] The transformation from more stable FCC or decahedral to icosahedral structures requires temperatures above the melting point, followed by rapid cooling (freezing) of the nanoparticle.[36,43] The melting point of gold nanoparticles is highly sensitive to size. Although the melting point of gold nanoparticles at ~2.6 nm in size is close to 500 K, an increase in size to 3 (or 4) nm causes the melting point to rise to ~750 K (or ~900 K).[37] This is consistent with the observations presented in Fig. 2. Given that the size of Au_{923} is ~3 nm and Au_{2057} ~ 4 nm, the temperature of 523 K employed does not approach sufficiently close to the melting point of the nanoparticles to induce an Ih-to-Dh structural transition, so even the least stable nanocluster isomer can survive the treatment.

Fig. 3 shows the proportions of size-selected Au_{923} and Au_{2057} nanocluster isomers, both before and after exposure to the full vapour-phase 1-pentyne hydrogenation reaction conditions. As shown in Fig. 3(a) and (b), with 9% Ih, 43% Dh and 35% FCC before the reaction, Au_{923} nanoclusters displayed similar stability to Au_{2057}: the relative proportions of Au_{923} isomers after treatment are 7% Ih, 45% Dh and 35% FCC. Such variations in isomer proportions fall within the (Poissonian) error. As shown in Fig. 3(c) the proportions of as-deposited Au_{2057} isomers before the reaction are 9% Ih, 54% Dh and 28% FCC. The isomer proportions were found to be almost identical post reaction (see Fig. 3(d)).

Although there is evidence for the chemisorption of 1-pentyne at the surface of bulk gold,[44] there are a limited number of investigations on the catalysis of 1-pentyne hydrogenation using gold. However, the hydrogenation of alkynes involving oxide-supported gold nanoparticles[27,29] suggests that, although there is higher selectivity to semi-hydrogenation with Au, gold catalysts are considerably less active than Pd.[28,29] For instance, TiO_2-supported gold nanoclusters of average size 4.7 nm are reported to show poor adsorption of alkyne or alkene species, suggesting there may be a weaker interaction between gold and 1-pentyne (as compared with Pd).

Fig. 4 shows the variation in the proportions of Pd_{2057} and Pd_{923} nanocluster isomers as a result of exposure to the 1-pentyne hydrogenation reaction conditions, which were exactly the same as in the case of the Au nanoclusters. Example images of the amorphous Pd_{923} and Pd_{2057} nanoclusters observed are shown in Fig. 4(a) and (d), respectively. Fig. 4(b) reveals that the vast majority (97%) of Pd_{923} nanoclusters initially exhibit an amorphous appearance; the only nanoclusters with an identifiable high symmetry structure (3%) are found to be Dh. After the reaction, as shown in Fig. 4(c), a large proportion (33%) of the nanoclusters could be assigned to a high symmetry structure, dominated by FCC (32%), leaving 1% as Dh. For Pd_{2057}, the proportion of amorphous nanoclusters pre-reaction is much lower at 37%, and almost a majority of the nanoclusters are FCC structures (see Fig. 4(e)). Both before and after reaction (Fig. 4(e) and (f)), more than three-quarters of the identified high symmetry isomers are assigned to be FCC.

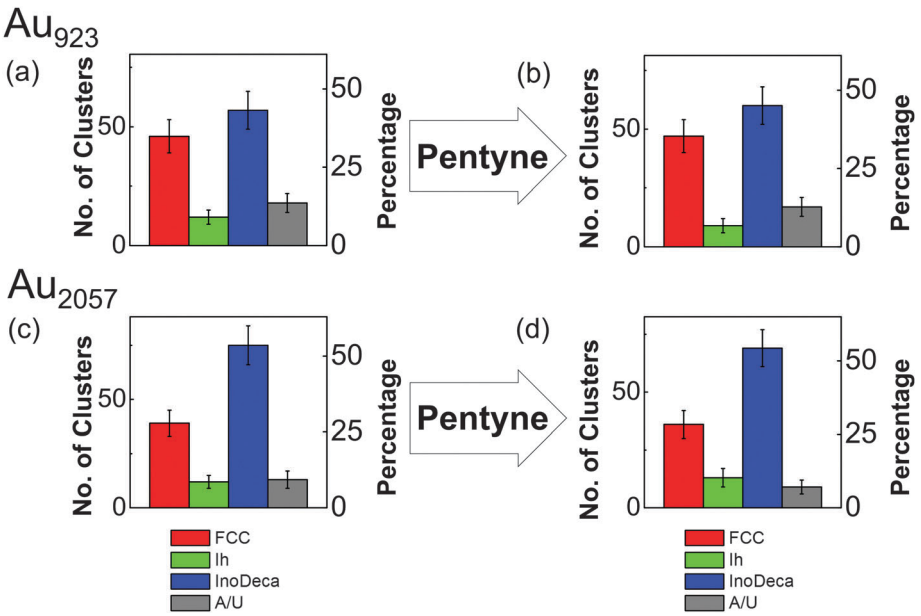

Fig. 3 (a, b) Charts showing the relative proportions of Au_{923} isomers (a) before and (b) after exposure to the reaction conditions for vapour-phase 1-pentyne hydrogenation. (c, d) Charts showing the relative proportions of Au_{2057} isomers (c) before and (d) after exposure to the same conditions. The reaction was conducted at 523 K for 2 hours (ramp rate of 2 °C min^{-1} from RT) with 1 M 1-pentyne in hexane vaporised by a carrier gas of 40% H_2 and 60% He (flow rate 247 ml min^{-1}). The cluster formation parameters were: condensation length, 250 mm; magnetron sputtering power, 10 W DC; condensation pressure, 0.60 mbar (Au_{923}) and 0.67 mbar (Au_{2057}); condensation gas flows, 200 sccm (Ar) and 150 sccm (He); deposition energy, 0.5 eV per atom.

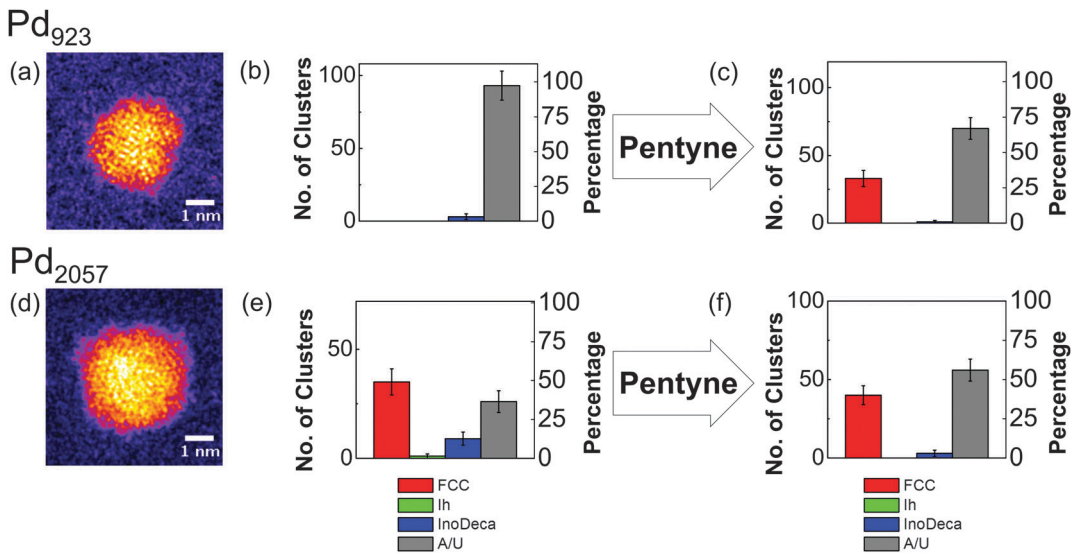

Fig. 4 (a, d) Example HAADF-STEM images of amorphous nanoclusters for (a) Pd_{923} and (d) Pd_{2057}, imaged prior to treatment. (b, c) Charts showing the relative proportions of Pd_{923} isomers (b) before and (c) after vapour-phase 1-pentyne hydrogenation treatment. (e, f) Charts showing the relative proportions of Pd_{2057} isomers both (e) before and (f) after the same treatment. The conditions for the treatments were identical to those for the Au nanoclusters shown in Fig. 3. Related cluster formation parameters: condensation length, 172 mm; magnetron sputtering power, 10 W DC; condensation pressure, 0.18 mbar (Pd_{923}) and 0.28 mbar (Pd_{2057}); condensation gas flows, 100 sccm (Ar) and 110 sccm (He); deposition energy, 0.9 eV per atom (Pd_{923}) and 0.4 eV per atom (Pd_{2057}).

Pd is known to oxidise spontaneously upon contact with oxygen,[31,45–47] but the oxidation depth on Pd single crystals is temperature dependent.[48] On the Pd(111) surface, PdO first forms as an amorphous layer, gradually increasing in crystallinity at elevated temperatures. When the temperature reaches 500 K, amorphous PdO layers coalescence to form a PdO(101) ad-layer with a thickness of 3.5 ML at saturation.[45,49] Oxygen can become incorporated into Pd nanoparticles in a number of ways, both at the surface and beneath, or through the formation of oxide shells.[50,51] For (oxide-supported) Pd nanoparticles with diameters of <5 nm, both oxidation and reduction by oxygen and hydrogen, respectively, proceed readily at room temperature.[52] For ZrO_2-supported PdO

nanoclusters with average size of 28 nm, shell-by-shell reduction in hydrogen has been observed and the clusters can be restored to Pd without fragmenting.[45] In the present case, the amorphous appearance of large proportions of both Pd_{2057} and, in particular, Pd_{923} nanoclusters, prior to the reaction, may therefore be attributable to surface oxidation in air, especially given storage conditions prior to imaging (desiccator, ambient temperature and pressure, 100 days). We note, however, that only 37% of Pd_{2057} nanoclusters observed before exposure to the reaction conditions appear to be amorphous, compared to 97% for Pd_{923} stored under identical conditions, which suggests that the Pd_{2057} nanoclusters exhibit a marked oxidation resistance as compared to Pd_{923}, a phenomenon that can be explored further in future work. It is possible that oxidised Pd nanoclusters can undergo reduction when exposed to the conditions of the 1-pentyne hydrogenation reaction, removing the oxide layer, and permitting the observation of (structural) motifs corresponding to high symmetry, ordered atomic structures in post-reaction HAADF-STEM imaging. As all Pd nanoclusters were stored under the same conditions both before and after the reaction, it implies that both Pd_{923} and Pd_{2057} nanoclusters are exhibiting a degree of oxidation resistance at room temperature and pressure post-reaction, at least for the high symmetry structural motifs observed. In particular, we note significant proportions of FCC structures for Pd_{2057} both before (49%) and after (40%) the reaction, as well as the emergence of FCC structures for Pd_{923} post-reaction. Indeed, the previous study of 1-pentyne hydrogenation with size-selected Pd nanoclusters suggested that there was no obvious change in the FCC-like structure of Pd_{400} following the reaction, although a full statistical analysis was not carried out. With regard to the present study, further investigation would be required to investigate fully the mechanisms involved and to verify whether the perceived oxidation resistance of the reduced Pd nanoclusters (post-reaction) arises due to changes to the intrinsic structure (to FCC), or results from deposits (due to surface adsorption) or carbonization (catalyst coking).

The ability to produce oxidised and oxidation-resistant Pd catalysts selectively may be advantageous,[53] particularly as there is some debate as to whether Pd or PdO is the more active catalyst. An example concerns the comparative activities of alumina-supported palladium for the combustion of methane,[54–56] for which early reports are conflicting. It is generally believed that methane oxidation proceeds rapidly through the chemisorption of oxygen onto PdO for alumina-supported Pd catalyst at atmospheric pressure.[56] Such chemisorption would cease on the Pd catalyst surface above 650 °C, which is the decomposition temperature of PdO, and hence the catalysed methane combustion stops.[55,56] Furthermore, in a more recent study conducted on a polycrystalline Pd plate in an ultrahigh vacuum system, the reaction rate of methane production drops drastically when the system goes beyond the decomposition temperature of PdO.[57]

4 Conclusions

We have reported an investigation into the effects of the 1-pentyne hydrogenation reaction, under realistic conditions, on the atomic structures of size-selected Au nanoclusters containing 923 ± 20 and 2057 ± 45 atoms, as well as Pd nanoclusters containing 923 ± 26 and 2057 ± 57 atoms. We find that both Au_{923} and Au_{2057} nanoclusters exhibit marked structural stability. The large majority of Pd_{923} nanoclusters were found to be amorphous in appearance before reaction, which may be attributable to surface oxidation. However, following exposure to the same reaction conditions, a significant proportion is found to exhibit high symmetry FCC structures, which may result from the reduction of the nanoclusters in hydrogen. Moreover, given the identical storage conditions before and after reaction, the observation of such structures implies a greater oxidation resistance post-reaction. We suggest that enhanced oxidation resistance may arise as a result of intrinsic structural changes or through protection of the surface due to carbonisation or surface absorption, but the exact origin would be the subject of further investigation. Au_{2057} nanoclusters, prepared under similar formation conditions to Au_{923}, are found to consist of a large proportion of FCC-like structures, both before and after the reaction, similar to Pd_{400} previously studied.

Acknowledgements

We acknowledge EPSRC and Johnson Matthey for funding this project. S.R.P. acknowledges support through a Science City Research Alliance Fellowship, funded by the Higher Education Funding Council for England (HEFCE).

References

1 M. Che and C. O. Bennett, *Adv. Catal.*, 1989, **36**, 55–172.
2 S. Vajda, M. J. Pellin, J. P. Greeley, C. L. Marshall, L. A. Curtiss, G. A. Ballentine, J. W. Elam, S. Catillon-Mucherie, P. C. Redfern, F. Mehmood and P. Zapol, *Nat. Mater.*, 2009, **8**, 213–216.
3 S. Lee, L. M. Molina, M. J. López, J. A. Alonso, B. Hammer, B. Lee, S. Seifert, R. E. Winans, J. W. Elam, M. J. Pellin and S. Vajda, *Angew. Chem., Int. Ed.*, 2009, **48**, 1467–1471.
4 Y. Le, F. Mehmood, S. Lee, J. Greeley, B. Lee, S. Seifert, R. E. Winansl, W. Elám, R. J. Meyer, P. C. Redfern, D. Teschner, R. l. Schlögl, M. J. Pellin, L. A. Curtiss and S. Vajda, *Science*, 2010, **328**, 224–228.
5 C. Harding, V. Habibpour, S. Kunz, A. N.-S. Farnbacher, U. Heiz, B. Yoon and U. Landman, *J. Am. Chem. Soc.*, 2009, **131**, 538–548.
6 S. Kunz, K. Hartl, M. Nesselberger, F. F. Schweinberger, G. Kwon, M. Hanzlik, K. J. J. Mayrhofer, U. Heiz and M. Arenz, *Phys. Chem. Chem. Phys.*, 2010, **12**, 10288–10291.
7 G. Sitja, S. L. Moal, M. Marsault, G. Hamm, F. Leroy and C. R. Henry, *Nano Lett.*, 2013, **13**, 1977–1982.
8 F. J. Perez-Alonso, D. N. McCarthy, A. Nierhoff, P. Hernandez-Fernandez, C. Strebel, I. E. L. Stephens, J. H. Nielsen and I. Chorkendorff, *Angew. Chem., Int. Ed.*, 2012, **51**, 4641–4643.

9 H. Falsig, B. Hvolbæk, I. S. Kristensen, T. Jiang, T. Bligaard, C. H. Christensen and J. K. Nørskov, *Angew. Chem.*, 2008, **120**, 4913–4917.
10 I. Lee, F. Delbecq, R. Morales, M. A. Albiter and F. Zaera, *Nat. Mater.*, 2009, **8**, 132–138.
11 S. B. Simonsen, I. Chorkendorff, S. Dahl, M. Skoglundh, J. Sehested and S. Helveg, *J. Am. Chem. Soc.*, 2010, **132**, 7968–7975.
12 S. R. Challa, A. T. Delariva, T. W. Hansen, S. Helveg, J. Sehested, P. L. Hansen, F. Garzon and A. K. Datye, *J. Am. Chem. Soc.*, 2011, **133**, 20672–20675.
13 T. Uchiyama, H. Yoshida, Y. Kuwauchi, S. Ichikawa, S. Shimada, M. Haruta and S. Takeda, *Angew. Chem., Int. Ed.*, 2011, **50**, 10157–10160.
14 G. Prieto, J. Zečević, H. Friedrich, K. P. De Jong and P. E. De Jongh, *Nat. Mater.*, 2013, **12**, 34–39.
15 F. Yang, M. S. Chen and D. W. Goodman, *J. Phys. Chem. C*, 2009, **113**, 254–260.
16 A. A. Herzing, C. J. Kiely, A. F. Carley, P. Landon and G. J. Hutchings, *Science*, 2008, **321**, 1331–1335.
17 A. Sanchez, S. Abbet, U. Heiz, W. D. Schneider, H. Hakkinen, R. N. Barnett and U. Landman, *J. Phys. Chem. A*, 1999, **103**, 9573–9578.
18 H.-G. Boyen, G. Kastle, F. Weigl, B. Koslowski, C. Dietrich, P. Ziemann, J. P. Spatz, S. Riethmuller, C. Hartmann, M. Moller, G. Schmid, M. G. Garnier and P. Oelhafen, *Science*, 2002, **297**, 1533–1536.
19 Z. Y. Li, N. P. Young, M. Di Vece, S. Palomba, R. E. Palmer, A. L. Bleloch, B. C. Curley, R. L. Johnston, J. Jiang and J. Yuan, *Nature*, 2008, **451**, 46–48.
20 Z. W. Wang and R. E. Palmer, *Nanoscale*, 2012, **4**, 4947–4949.
21 Z. W. Wang and R. E. Palmer, *Nano Lett.*, 2012, **12**, 5510–5514.
22 Z. W. Wang and R. E. Palmer, *Phys. Rev. Lett.*, 2012, **108**, 245502.
23 S. R. Plant, L. Cao, F. Yin, Z. W. Wang and R. E. Palmer, *Nanoscale*, 2014, **6**, 1258–1263.
24 S. R. Plant, L. Cao and R. E. Palmer, *J. Am. Chem. Soc.*, 2014, **136**, 7559–7562.
25 F. Yin, S. Lee, A. Abdela, S. Vajda and R. E. Palmer, *J. Chem. Phys.*, 2011, **134**, 141101.
26 V. Habibpour, M. Y. Song, Z. W. Wang, J. Cookson, C. M. Brown, P. T. Bishop and R. E. Palmer, *J. Phys. Chem. C*, 2012, **116**, 26295–26299.
27 J. A. Lopez-Sanchez and D. Lennon, *Appl. Catal., A*, 2005, **291**, 230–237.
28 L. McEwan, M. Julius, S. Roberts and J. C. Q. Fletcher, *Gold Bull.*, 2010, **43**, 298–306.
29 Y. Segura, N. Lopez and J. Perezramirez, *J. Catal.*, 2007, **247**, 383–386.
30 M. W. Tew, M. Nachtegaal, M. Janousch, T. Huthwelker and J. A. van Bokhoven, *Phys. Chem. Chem. Phys.*, 2012, **14**, 5761–5768.
31 D. Teschner, E. Vass, M. Hävecker, S. Zafeiratos, P. Schnörch, H. Sauer, A. Knop-Gericke, R. Schlögl, M. Chamam, A. Wootsch, A. S. Canning, J. J. Gamman, S. D. Jackson, J. McGregor and L. F. Gladden, *J. Catal.*, 2006, **242**, 26–37.
32 D. Teschner, J. Borsodi, A. Wootsch, Z. Révay, M. Hävecker, A. Knop-Gericke, S. D. Jackson and R. Schlögl, *Science*, 2008, **320**, 86–89.
33 M. W. Tew, H. Emerich and J. A. van Bokhoven, *J. Phys. Chem. C*, 2011, **115**, 8457–8465.
34 P. Albers, J. Pietsch and S. F. Parker, *J. Mol. Catal. A: Chem.*, 2001, **173**, 275–286.
35 Y. Li, H. Cheng, T. Yao, Z. Sun, W. Yan, Y. Jiang, Y. Xie, Y. Sun, Y. Huang, S. Liu, J. Zhang, Y. Xie, T. Hu, L. Yang, Z. Wu and S. Wei, *J. Am. Chem. Soc.*, 2012, **134**, 17997–18003.
36 K. Koga, T. Ikeshoji and K. Sugawara, *Phys. Rev. Lett.*, 2004, **92**, 2–5.
37 P. Buffat and J. P. Borel, *Phys. Rev. A: At., Mol., Opt. Phys.*, 1976, **13**, 2287.
38 I. M. Goldby, B. von Issendorff, L. Kuipers and R. E. Palmer, *Rev. Sci. Instrum.*, 1997, **68**, 3327–3334.
39 S. Pratontep, S. J. Carroll, C. Xirouchaki, M. Streun and R. E. Palmer, *Rev. Sci. Instrum.*, 2005, **76**, 045103.
40 B. von Issendorff and R. E. Palmer, *Rev. Sci. Instrum.*, 1999, **70**, 4497–4501.
41 Z. W. Wang, O. Toikkanen, B. M. Quinn and R. E. Palmer, *Small*, 2011, **7**, 1542–1545.
42 C. Koch, PhD thesis, Arizona Sate University, 2002.
43 C. Cleveland, W. Luedtke and U. Landman, *Phys. Rev. B: Condens. Matter Mater. Phys.*, 1999, **60**, 5065–5077.
44 H. Feilchenfeld and M. J. Weaver, *J. Phys. Chem.*, 1989, **93**, 4276–4282.
45 S. C. Su, J. N. Carstens and A. T. Bell, *J. Catal.*, 1998, **176**, 125–135.
46 E. Voogt, A. J. M. Mens, O. L. J. Gijzeman and J. W. Geus, *Catal. Today*, 1999, **47**, 321–323.
47 D. Zemlyanov, B. Klötzer and H. Gabasch, *Top. Catal.*, 2013, **56**, 885–895.
48 X. Guo, A. Hoffman and J. T. Yates, *J. Chem. Phys.*, 1989, **90**, 5787.
49 H. H. Kan and J. F. Weaver, *Surf. Sci.*, 2009, **603**, 2671–2682.
50 T. Schalow, B. Brandt, D. Starr, M. Laurin, S. Shaikhutdinov, S. Schauermann, J. Libuda and H.-J. Freund, *Angew. Chem., Int. Ed.*, 2006, **45**, 3693–3697.
51 I. Meusel, J. Hoffmann, J. Hartmann, M. Heemeier, M. Bäumer, J. Libuda and H.-J. Freund, *Catal. Lett.*, 2001, **71**, 5–13.
52 A. Baylet, P. Marécot, D. Duprez, P. Castellazzi, G. Groppi and P. Forzatti, *Phys. Chem. Chem. Phys.*, 2011, **13**, 4607–4613.
53 S. M. Lang, I. Fleischer, T. M. Bernhardt, R. N. Barnett and U. Landman, *J. Am. Chem. Soc.*, 2012, **134**, 20654–20659.
54 M. Lyubovsky and L. Pfefferle, *Catal. Today*, 1999, **47**, 29–44.
55 R. Burch and F. J. Urbano, *Appl. Catal., A*, 1995, **124**, 121–138.
56 R. J. Farrauto, M. C. Hobson, T. Kennelly and E. M. Waterman, *Appl. Catal., A*, 1992, **81**, 227–237.
57 G. Zhu, J. Han, D. Y. Zemlyanov and F. H. Ribeiro, *J. Phys. Chem. B*, 2005, **109**, 2331–2337.